Effect of angle of attack on aerodynamic characteristics of levitated freestream-aligned circular cylinder

Sho Yokota,* Keisuke Asai, and Taku Nonomura
Department of Aerospace Engineering, Graduate School of Engineering, Tohoku University, 6-6-01 Aramaki-aza Aoba, Aoba-ku, Sendai, Miyagi 980-8579, Japan

(Received 15 August 2022; accepted 2 February 2023; published 13 February 2023)

An effect of an angle of attack on the aerodynamic characteristics of a freestream-aligned circular cylinder is investigated and discussed. The experiment without support interference was conducted using a magnetic suspension and balance system (MSBS) which can levitate and support a model. A cylindrical model with a fineness ratio of 1.0 was employed in wind tunnel tests. The Reynolds numbers based on the diameter of the model were 3.3×10^4 and 6.7×10^4. The range of the angle of attack is from 0 to 15°. Aerodynamic forces and velocity fields were obtained by the MSBS and particle image velocimetry. The results of the time-averaged aerodynamic force and moment coefficients and the time-averaged velocity field illustrate that the flow reattachment occurs at an angle of 9° or more. The flow reattachment changes the aerodynamic characteristics, especially the lift and pitching moment coefficients and the lift force fluctuations.

DOI: 10.1103/PhysRevFluids.8.024701

I. INTRODUCTION

Bluff bodies which are nonstreamline-shaped objects are applied in an industrial field in many cases. Applications range widely from transportation machines such as trains, buses, and trucks to containers and buildings. Various geometries are included in a bluff body such as a circular cylinder, a rectangular cylinder, and a sphere [1]. A freestream-aligned circular cylinder is also one of the bluff bodies. A circular cylinder in which the flat surface is perpendicular to the freestream is called a freestream-aligned circular cylinder. Applications with an outer shape similar to the freestream-aligned circular cylinder are an oil drum, an engine canister, a reentry capsule, and so on. These structures are connected to trucks or helicopters, or work themselves. Since these are moved in fluids, comprehension of aerodynamic characteristics is quite important in terms of the stability of transportation. Although many experimental studies have been conducted for the bluff bodies, a mechanical supporting device such as a strut and wires is applied for supporting a model in a test section in almost all cases. However, the mechanical supporting device interferes with the flow around the model, which is called support interference. The support interference is desired to be eliminated for clarifying fluid phenomena.

The wind tunnel test using a magnetic suspension and balance system (MSBS) is one of the experimental methods without support interference. The MSBS uses magnetic forces for levitating and supporting a model. Therefore, there is no object except the model in the test section. Experimental investigations for the freestream-aligned circular cylinder using the MSBS have been conducted in recent years [2–8]. Higuchi *et al.* [3] and Yokota *et al.* [6] showed that the flow field around the freestream-aligned circular cylinder is changed due to the fineness ratio L/D from the results of the time-averaged velocity fields measured by particle image velocimetry (PIV), where L

*sho.yokota.r1@dc.tohoku.ac.jp

and D are the length and diameter of the circular cylinder model, respectively. The flow separates at the leading edge not depending on L/D, but the separated shear layer does not reattach to the curved surface of the cylinder in the case of $L/D < 1.5$. In contrast, the shear layer reattaches to the curved surface in the case of $L/D \geqslant 1.5$. Moreover, the curve of the time-averaged drag coefficient and base pressure coefficient shows the minimum at approximately $L/D = 1.7$. This suggests that the shear layer reattachment strongly relates to the aerodynamic forces acting on the cylinder.

Three characteristic flow structures are observed around the freestream-aligned circular cylinder: recirculation bubble pumping, large-scale vortex shedding, and Kelvin-Helmholtz instability [1,6,8]. The recirculation bubble pumping is observed in the nonreattaching flow with $L/D < 1.5$ and the fluctuation frequency is at $\mathrm{St} \approx 0.02$. Here, the Strouhal number is defined as $\mathrm{St} = \frac{fD}{U}$, where f is a frequency. This structure affects drag force and base pressure, which show relatively large fluctuations at a similar frequency. Second, the large-scale vortex shedding is a phenomenon observed for $L/D \leqslant 1.5$ and does not appear for $L/D = 2.0$, which is the case where the shear layer constantly reattaches. The frequency of fluctuations is $\mathrm{St} \approx 0.14$, and the lateral aerodynamic force fluctuations appear at the same frequency. These two structures are flow structures behind the cylinder and are considered to be affected by the reattachment of the shear layer to the side of the cylinder. In contrast, the Kelvin-Helmholtz instability appears near the leading edge of the cylinder and does not differ greatly, depending on L/D.

Up to this point, we have described that L/D determines whether the shear layer reattaches or not, resulting in changes in time-averaged aerodynamic force coefficients and flow structure. However, the behavior of the shear layer is known to be affected not only by the fineness ratio L/D but also by the angle of attack α. Prosser [9] numerically investigated the aerodynamic characteristics of circular cylinders with $L/D = 1.0$ and 2.0 while changing α. An interesting variation of the flow structure is seen in the case of $L/D = 1.0$. At $\alpha = 0^\circ$, the shear layer does not reattach on the curved surface of the cylinder as described above, resulting in the nonreattaching flow. Note that the angle of attack of 0° is the attitude in which the flat surface of the cylinder is perpendicular to the freestream, which is 90° different from the definition of the angle of attack in Prosser's paper [9]. As α increases to some extent, the flow is fully attached to the flat surface as in the 0° case, while the shear layer reattaches on the windward curved surface and does not on the leeward curved surface. Here, the windward and leeward curved surfaces are defined as the bottom and top halves of the curved surface of the cylinder when $\alpha = 0^\circ$, respectively. When α further increases, the flow becomes fully attached to the windward curved surface and the flow reattachment occurs on the flat surface. The flow reattaches on both of the flat surfaces in the case of $\alpha = 90^\circ$. In addition to the flow structure, the vortex shedding frequency and time-averaged aerodynamic forces and moments have also been reported to be affected by the angle of attack [9]. Prosser [9] showed that the side force coefficients change at $\alpha = 10$–20°, suggesting that the flow separated at the leading edge reattaches on the windward curved surface at $\alpha \approx 10^\circ$ angle of attack. However, the results of the aerodynamic forces were obtained only every 10° in the study, and there has been no detailed study of the angle of attack at which reattachment occurs. Since the angle of attack sensitively affects the aerodynamic characteristics of the freestream-aligned circular cylinder, it is important to clarify the angle of attack at which shear layer reattachment occurs and what difference it makes.

The main objectives of the present paper are to identify the angle of attack α when the reattachment of the flow separated at the leading edge of the cylinder appears and to clarify the effect of α on the flow field and the aerodynamic force and moment. Experiments were conducted under conditions that did not interfere with the flow by magnetically supporting a freestream-aligned circular cylinder and measuring the velocity field around the cylinder using PIV measurements. The aerodynamic forces and moments were simultaneously measured with the PIV measurements using the balance function of the MSBS.

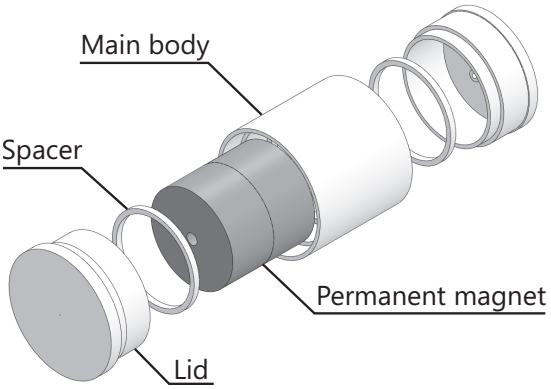

FIG. 1. The schematic of the cylindrical model.

II. EXPERIMENTAL SETUP

A. Cylindrical model

A cylindrical model with $L/D = 1.0$ was used, and the transition from a flow field in which the flow is completely separated to one in which the flow reattaches was captured by changing the angle of attack. The flow around a freestream-aligned circular cylinder with an angle of attack of 0° is known to be nonreattaching flow which does not involve shear layer reattachment [6,10].

Figure 1 shows a schematic of the cylindrical model used. The model is made of polyoxymethylene and the diameter of the cylinder D is 50 mm. As described in Sec. II B, the cross section of the measurement section is 0.3 m square, resulting in a blockage ratio of 2.2% in the wind tunnel test. Since the blockage ratio is low, any correction has not been applied to the aerodynamic force and moment coefficients. The model is white with a black marker applied on the center of the lengthwise direction. This marker is employed for the detection of the model position by the sensor subsystem of 0.3-m MSBS. Two neodymium magnets with an outer diameter of 40 mm, an inner diameter of 5 mm, and a length of 20 mm were inserted inside the model. In the wind tunnel test, the angle of attack of the cylindrical model was set in 1° increments from 0 to 15°.

Next, the coordinate system is introduced. The coordinate system is defined based on the cylinder with the central axis parallel to the freestream, as shown in Fig. 2. The origin is the center of the base of the cylinder, with the x axis in the freestream direction, the z axis in the vertically upward direction, and the y axis to form a right-handed coordinate system. The pitch, yaw, and roll angles, θ,

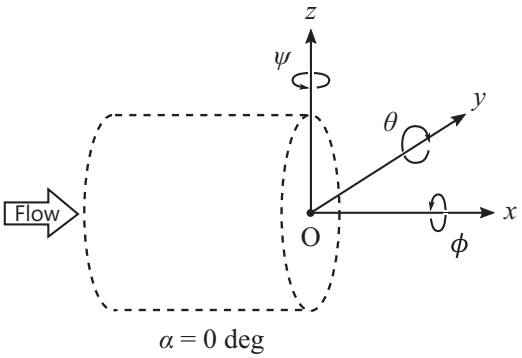

FIG. 2. The coordinate system.

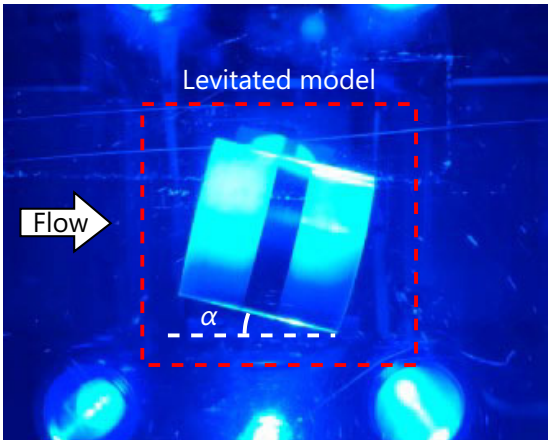

FIG. 3. The levitated cylindrical model at $\alpha = 15^\circ$ in the 0.3-m MSBS. The freestream direction is from left to right.

ψ, and ϕ, are defined as the angles around the y, z, and x axes, respectively. Note that the coordinate system differs from that of Prosser [9] by 90° in the yaw direction.

B. Wind tunnel

The Tohoku-University Basic Aerodynamic Research Tunnel (T-BART) was employed in wind tunnel tests. T-BART is a suction-type wind tunnel with a closed test section. The cross section of the test section is a square with 0.3 m on a side. The freestream velocity range is 5–60 m/s and the turbulence intensity is less than 0.5%. The freestream velocity U was set to 10 and 20 m/s for the wind tunnel tests. The Reynolds number with the cylinder diameter D as the reference length is calculated by the following equation:

$$\mathrm{Re}_D = \frac{UD}{\nu}, \tag{1}$$

where ν is the kinematic viscosity, which is 1.512×10^{-5} m^2/s for air at 20 °C. The Reynolds numbers calculated by Eq. (1) are 3.3×10^4 and 6.7×10^4.

C. Magnetic suspension and balance system

The 0.3-m MSBS at Tohoku University was used as a support device for the model. An MSBS consists of a sensor subsystem, a coil subsystem, and a control subsystem. The model is levitated and supported by the interaction between the magnetic field generated by the coil subsystem and the permanent magnets inside the model, as shown in Fig. 3. The coil subsystem consists of ten electromagnets, eight of which are iron-cored coils and the remaining two are air-cored coils. These coils are placed around the wind tunnel test section, and the position and attitude of the model can be maintained by controlling the value of the electric current applied to the coils. The electric current applied to the coil is determined by feedback control based on the position and attitude of the model. The sensor subsystem is responsible for monitoring the model and consists of five CCD line sensors, blue LED light sources, half-mirrors, short-pass optical filters, and plano-convex lenses. Edges and markers of the model are detected from the image acquired by the CCD line sensors, and the model position and attitude are calculated. Based on this information, feedback control is performed by a control subsystem that mainly employs proportional-integral control and includes a double-phase advance compensator. The control frequency was set to 1250 Hz. The equipment of the MSBS in the present study is the same as that in the previous study [6].

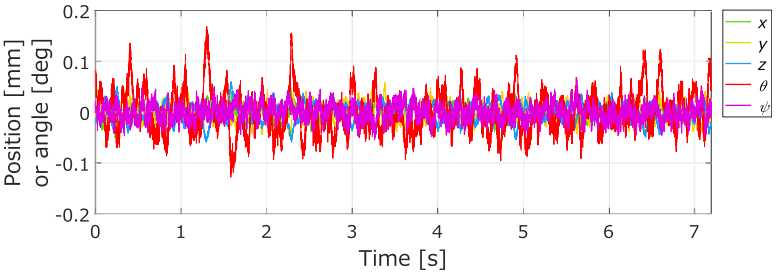

FIG. 4. The positional fluctuations of the levitated cylindrical model at $\alpha = 15^\circ$ and $\mathrm{Re}_D = 6.7\times10^4$.

The 0.3-m MSBS is capable of six-degree-of-freedom position and attitude control [11,12], but five-degree-of-freedom contro,l excluding roll, was performed in the wind tunnel test because the freestream-aligned circular cylinder is axisymmetric to the flow. Figure 4 shows the positional fluctuations in each direction in a measurement at $\alpha = 15^\circ$ and $\mathrm{Re}_D = 6.7\times10^4$. The fluctuations in the pitching direction are larger than in the other directions, but they are within $\pm0.2^\circ$. Furthermore, the root-mean-square value of them is 0.041°. Since the value is quite small, the oscillation is assumed to be negligible. The rolls were confirmed not to rotate significantly during the wind tunnel test. Refer to Yokota *et al.* [6] for more details of the levitation principle and each subsystem, as well as the preparatory tests before the wind tunnel tests. Here, some differences from the previous study [6] in the preparatory tests are introduced. The sensor calibration which calculates the relationship between the model position and the pixel number on the CCD line sensors was performed in the range of the pitching angle from -0.5 to 15.5°. This range includes the angle of attack in the wind tunnel test. Accordingly, the search range of the pitching angle in the attitude angle adjustment was reduced to the range of -0.5 to 0.5°. The pitch angle correction obtained from this adjustment was 0.105°. Therefore, the influence of a small calibration range in the negative pitching direction did not appear in the test.

D. Particle image velocimetry

PIV was adopted and velocity fields were measured. Figure 5 shows a schematic of the optical setup for the PIV measurements. The optical system was configured with a high-speed camera (Phantom v2640, Vision Research), a single-focus lens (Micro-Nikkor 105 mm f/2.8), band-pass optical filter (527 ± 10 nm, Edmund Optics), and Nd:YLF laser (LDY-303PIV, Litron). The pixel size, number of pixels, and bit depth of the camera are 13.5 μm, 2048×1952, and 12 bit, respectively. Microparticulated dioctyl sebacate was used as tracer particles.

The setup in the wind tunnel test is the same as the study by Yokota *et al.* [8], and their report shows that the tracer particles have sufficient followability. The laser illuminated the xz plane through the central axis of the cylinder from the downstream side. The high-speed camera was placed between the coils of the MSBS as shown in Fig. 5. The field of view (FOV) was adjusted to obtain velocity fields near the side of the cylinder where the flow is expected to reattach. The camera was arranged to vertically face the laser sheet, and the FOV was not changed with the angle of attack of the model. Velocity fields were measured at $\alpha = 0$, 3, 6, 8, 9, 10, 11, 12, and 15°. A fine setting of α around 10° where flow reattachment was expected to occur was employed. The sampling rates of the PIV measurements were 400 and 800 Hz at 10 and 20 m/s, respectively. Although 6301 image pairs were acquired in a run, the initial image pairs for approximately 0.3 s were not used for analyses because the laser power was not sufficient immediately after the start of the measurement. The measurement was performed five times for each condition, and a sufficiently large amount of the velocity field data was obtained for the analyses. The analyses of the acquired particle images are described in Sec. III A.

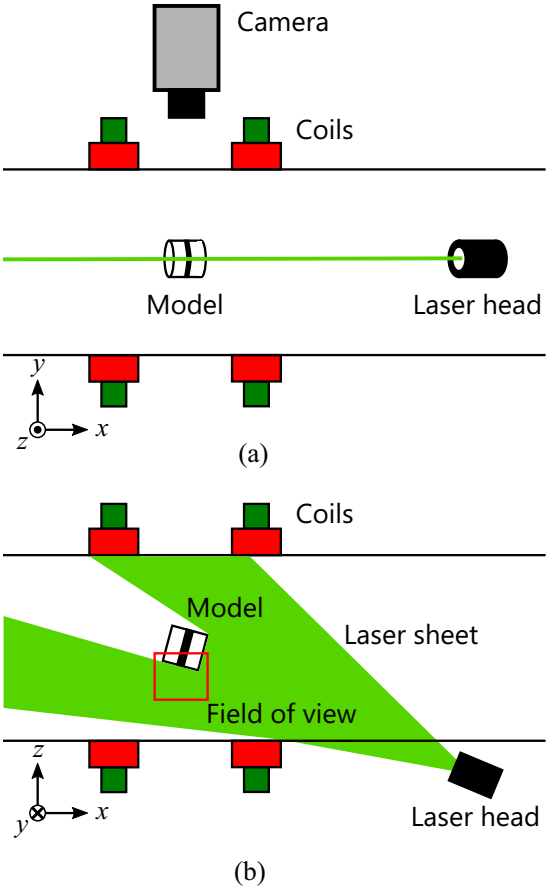

FIG. 5. The schematics of the optical configuration for the PIV measurements from (a) top and (b) side.

III. ANALYSIS

A. Velocity field

Instantaneous velocity fields and time-averaged velocity fields were, respectively, calculated using the conventional spatial correlation (CSC) method and the single-pixel ensemble correlation (SPC) method, as with the previous study of Yokota *et al.* [8]. These methods were developed by Willert and Gharib [13] and Westerweel *et al.* [14], respectively, and applied to several practical flows [15,16] with improvement for turbulent statistics [17,18]. The SPC method with its high spatial resolution of the obtained velocity field is highly significant because the angle of attack α at which the flow separated at the leading edge reattaches is identified from the time-averaged velocity field.

Instantaneous velocity fields were calculated using the analysis software (Dynamic Studio 7.5, Dantec Dynamics). First, the model areas on the particle image and region that were not illuminated by the laser were masked. Next, the background image was calculated from the time series of the particle images, and background subtraction was performed. The image was trimmed into 2048 px$\times$1200 px by removing the freestream region observed in the image. The analysis using the CSC method was applied to the processed particle images. The recursive correlation method is employed in this process. The initial interrogation window was 32 px$\times$32 px and the final correlation window size was reduced to 8 px$\times$8 px. The number of particles in the final interrogation

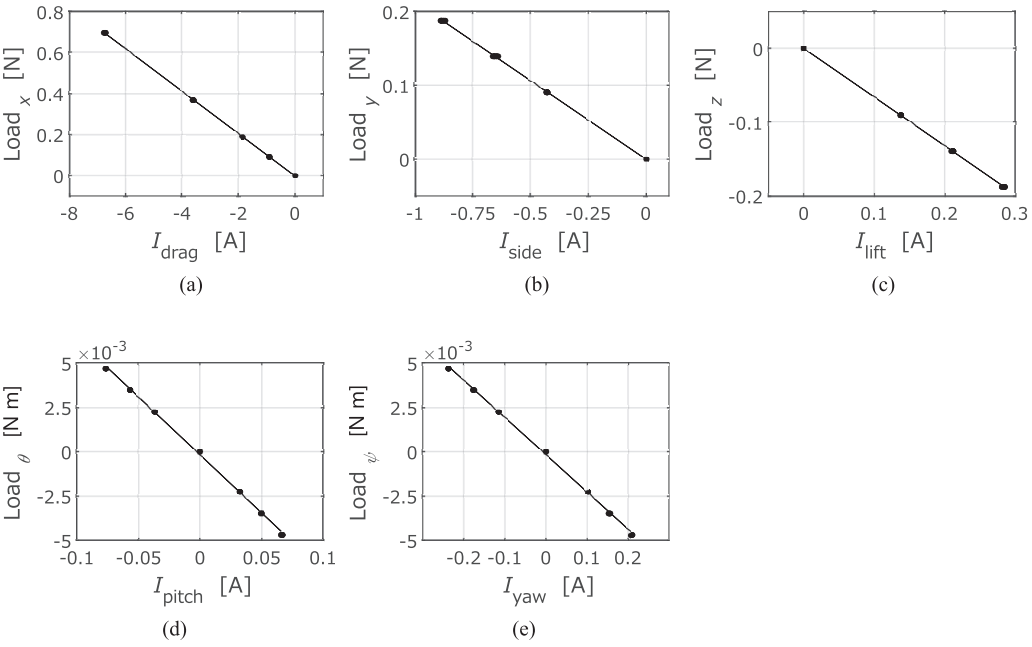

FIG. 6. The results of the force calibration test for (a) x, (b) y, (c) z, (d) pitch, and (e) yaw direction.

window of 8 px×8 px was 3.98, which corresponds to 63.7 particles in the initial interrogation window of 32 px×32 px. The number of particles within the initial interrogation window was sufficient, and the recursive correlation method was employed, resulting in a percentage of error vectors of 0.66%. The error vector processing was performed on the velocity field obtained from the analysis above, and the velocity field after this processing was treated as an instantaneous velocity field. The distance between adjacent vectors is 232 μm.

The time-averaged velocity fields were calculated using MATLAB code. Twenty-thousand pairs of particle images were used for the analysis, regardless of the freestream velocity. This amount corresponds to 50 s at 10 m/s and 25 s at 20 m/s. Therefore, the obtained velocity fields are considered to be averaged in a sufficiently long time. The obtained velocity fields are highly continuous and, therefore, no error vector processing was applied. The distance between adjacent vectors is 29 μm. which is 1/8 of that for the CSC method.

The uncertainty of the time-averaged and instantaneous velocity field was calculated, and the results are shown in Appendix A. The uncertainty is low in both analysis methods, regardless of the high-speed region in the freestream and the low-speed region inside the shear layer. Therefore, it should not alter the conclusions of the present paper.

B. Aerodynamic force

Aerodynamic forces and moments acting on the cylindrical model are measured using the balance function of the MSBS. The force calibration test is performed for this measurement before the wind tunnel tests. In the calibration test, loads with known weights are applied to the levitated model, and the electric current values for generating a magnetic force are simultaneously measured. Figure 6 shows that the relationship between the forces and the electric current values is almost linear. Refer to the paper by Yokota *et al.* [6] for more details on the force calibration test and the calculation of the aerodynamic forces in the 0.3-m MSBS.

Since the cylindrical model had angles to the coordinate system of the MSBS in the experiments, the calibration coefficient in the case $\alpha = 0^\circ$ cannot be applied, as it is when the forces and moments

in the case of $\alpha \neq 0^\circ$ are calculated. However, the straightforward calibration test for the cylinder at $\alpha \neq 0^\circ$ is quite difficult to conduct. Senda *et al.* [19] suggested the method of the evaluation of the aerodynamic forces and moments using the calibration coefficient at $\alpha = 0^\circ$ by applying the correction, and showed that evaluation errors are within approximately 4% up to $\alpha = 40^\circ$. The method suggested by Senda *et al.* [19] was adopted and the aerodynamic forces and moments were evaluated in the present paper. The calculation is described in Appendix C. For further details, refer to the paper by Senda *et al.* [19].

The forces and moments were nondimensionalized using Eqs. (2) and (3),

$$C_{\text{force}} = \frac{2F}{\rho U^2 S}, \tag{2}$$

$$C_{\text{moment}} = \frac{4N}{\rho U^2 L S}, \tag{3}$$

where C, F, N, ρ, and S are the coefficients of the force or the moment, the force, the moment, the density of air, and the projection area onto yz plane, respectively. The time-averaged aerodynamic force and moment coefficients are calculated by substituting $\overline{F}$ and $\overline{N}$ to Eqs. (2) and (3), respectively. Here, a correction for the blockage effect was not applied to the coefficients. On the other hand, the inertial force is taken into account for analyzing the aerodynamic force fluctuations as with the previous study [6]. The inertial force is subtracted from the magnetic force when calculating the amplitude spectrum. Therefore, the oscillation of the model in the wind tunnel test as mentioned in Sec. II C was removed.

Details of the calculation for the uncertainty of time-averaged aerodynamic force and moment coefficients are summarized in Appendix B. The uncertainty appears in the results in Sec. IV A 2.

IV. RESULTS AND DISCUSSIONS

A. Time-averaged aerodynamic characteristics

1. Time-averaged velocity fields

Figure 7 shows the time-averaged velocity fields of the streamwise component with streamlines in the case of $\mathrm{Re}_D = 3.3\times10^4$. The velocity is nondimensionalized using the freestream velocity U. The flow field is significantly changed with α. First, the recirculation region formed on the side of the curved surface of the cylinder becomes smaller as α increases. Furthermore, the region with the positive streamwise velocity is observed near the leading edge of the cylinder. This is considered to be caused by the three-dimensionality of the flow due to the nonaxisymmetric flow. However, the comprehension of the entire flow around the inclined circular cylinder is impossible from only the results in the measurement plane. Therefore, an accurate understanding of the three-dimensional change in the flow field by α cannot be developed.

The existence of the reattachment of the flow separated at the leading edge on the windward curved surface can be confirmed from these results. Figure 8 shows the time-averaged velocity fields in the vicinity of the trailing edge at $\alpha = 8$ and 9°. The reattachment of the flow is judged by the presence or absence of the separation at the trailing edge of the flow on the cylinder base. The flow on the base induced by the recirculation region behind the cylinder is separated at the trailing edge in the case of $\alpha = 8^\circ$, as shown in Fig. 8(a). This implies that the flow separated at the leading edge does not reattach on the windward curved surface. Therefore, the nonreattaching flow occurs in the case of $\alpha \leqslant 8^\circ$. In contrast, the flow on the base is not separated at the trailing edge in the case of $\alpha = 9^\circ$, as shown in Fig. 8(b). The result indicates that the separated flow reattaches on the windward curved surface of the cylinder. Subsequently, the reattaching flow occurs in the case of $\alpha \geqslant 9^\circ$.

The change in the flow field due to α has been discussed in this section. Three flow regimes on the cylinder surface have been reported by Prosser: fully separated flow, reattaching flow, and fully attached flow [9]. Two regimes are observed on the windward curved surface focused in the range

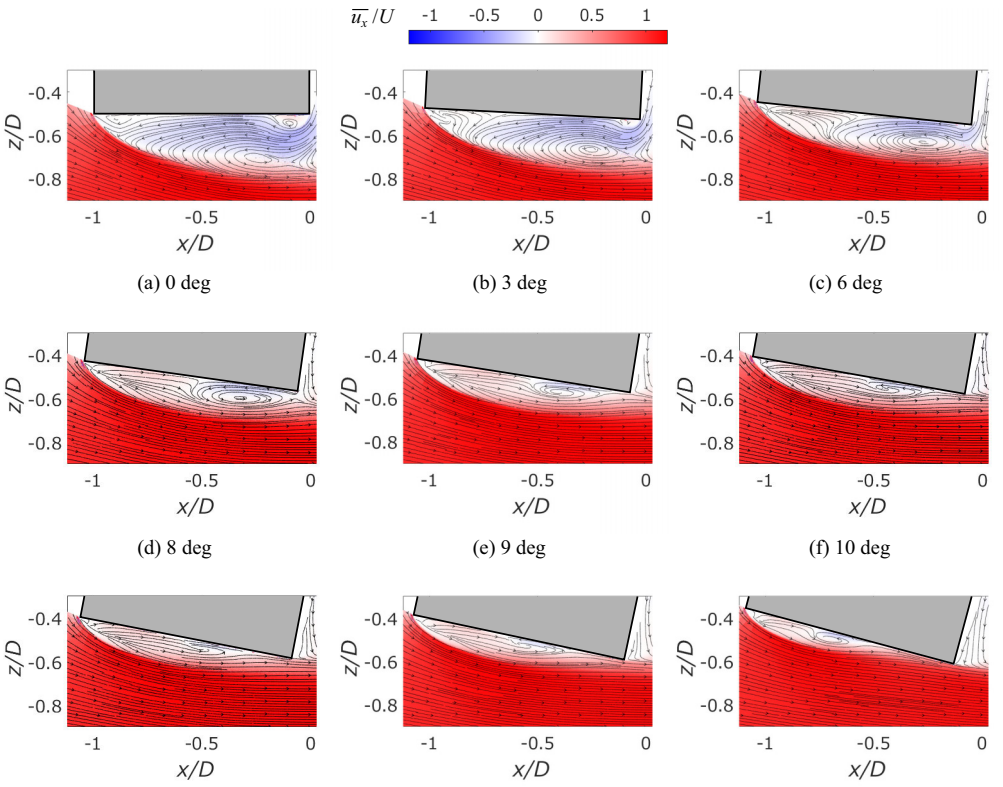

FIG. 7. The time-averaged velocity fields from (a) 0–(i) 15° at $\mathrm{Re}_D = 3.3\times10^4$. Black lines with arrows in the figures represent the streamlines.

of $\alpha = 0$–15°. The cases of α of 0–8° and 9–15° correspond to the regimes of fully separated flow and reattaching flow, respectively. The effect of α and the flow reattachment on the time-averaged aerodynamic forces and moment is discussed in Sec. IV A 2.

2. Time-averaged aerodynamic force and moment

The previous study by Prosser [9] showed the three flow regimes on the curved surface of the cylinder and the drag, side force, and yawing moment coefficients for the circular cylinder which, respectively, correspond to the drag, lift, and pitching moment in the present paper. The following changes in the force and moment coefficients by the flow reattachment on the windward curved surface are expected to be observed. The drag coefficient is expected to decrease with increasing α, with no difference due to the change in the flow regime. The lift coefficient is expected to decrease with increasing α in the range of 8–9°, corresponding to the regime of fully separated flow, but it is expected to increase by increasing α in the range of 9–15°, corresponding to the regime of reattaching flow. The pitching moment coefficient is considered to decrease with increasing α in the range of the present paper. The slope of the curve is expected to slightly differ in the case of fully separated flow and reattaching flow. The greater slope will be observed in the range of 9–15°, which corresponds to the flow regime of reattaching flow.

Figure 9 shows the time-averaged drag, lift, and pitching moment coefficients, C_{drag}, C_{lift}, and C_{pitch} without the correction for the blockage effect. Here, C_{drag} and C_{lift} were calculated by substituting F_x and F_z into Eq. (2), respectively. The pitching moment coefficient C_{pitch} was calculated

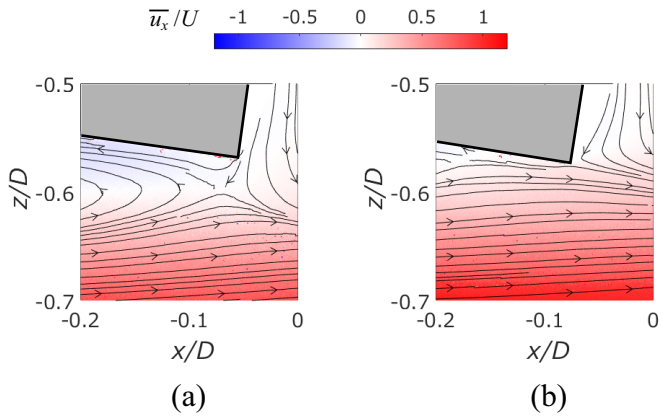

FIG. 8. The time-averaged velocity fields in vicinity of the trailing edge at (a) 8° and (b) 9° at $\mathrm{Re}_D = 3.3\times10^4$.

from N_y using Eq. (3). The red and blue points represent the results in the case of $\mathrm{Re}_D = 3.3\times10^4$ and 6.7×10^4, respectively. The error bars on the points represent the uncertainty of the coefficients shown in Appendix B. In contrast, the black points are the values taken from the results in Prosser's work [9]. Here, the reference area was changed to S from LD used in his work. In addition, the broken line in each figure is arranged between $\alpha = 8$ and 9°, where the flow state switches from the nonreattaching flow to the reattaching flow.

The curves of C_{lift} and C_{pitch} shown by Prosser [9] are similar to those in the present paper, as shown in Figs. 9(b) and 9(c). However, the difference for C_{drag} between the case of the present and previous studies is high except with $\alpha = 0°$. Furthermore, not shown here, the curves for the three-dimensional square cylinder with $L{:}W{:}H = 1{:}1{:}1$, which are shown in the paper of Greenwell [20], are quite similar to the case of the circular cylinder with $L/D = 1.0$, where W and H are the width and the height of the cylinder. The aerodynamic characteristics of a three-dimensional rectangular cylinder, moreover, closely resemble those of a two-dimensional rectangular cylinder. Since the pressure distribution on the surface of the cylinder was not obtained, the discussion is based on the results of previous studies. The following discussion refers to reports on the aerodynamic

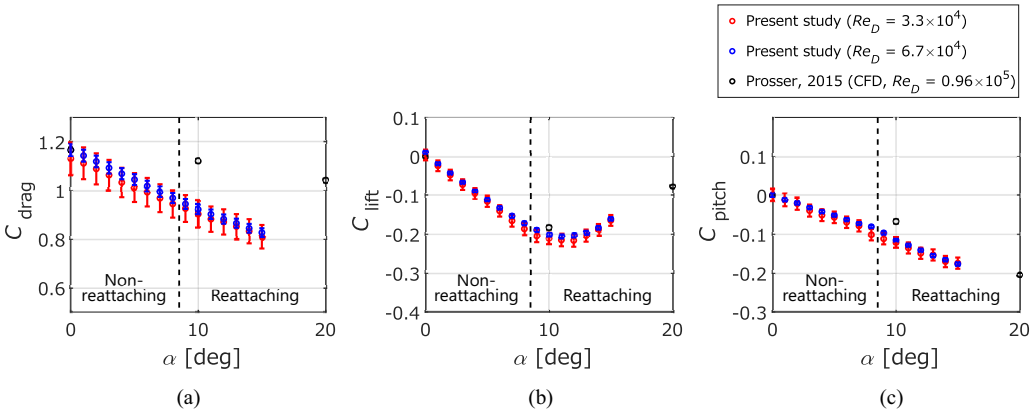

FIG. 9. The time-averaged (a) drag, (b) lift, and (c) pitching moment coefficients. The broken line in each figure represents the border of the states of the nonreattaching flow and the reattaching flow.

characteristics of disks, cylinders, three-dimensional square cylinders, and two-dimensional square cylinders.

Figure 9(a) shows that C_{drag} decreases as α increases. However, the negative slope is greater than that in the case of Prosser's work. The absolute value of C_{drag} at $\alpha = 10^\circ$ is 21.5% higher in the previous study than in the present paper. The drag coefficient when $\alpha = 0^\circ$ varies with L/D because the pressure distribution at the front does not depend on L/D, but the negative pressure generated by the circulation in the recirculation region formed behind the cylinder base varies with L/D in the case of $L/D \leqslant 1.5$ [6]. On the other hand, the change in the drag coefficient with α is caused by the combined effect of the change in pressure distribution at the front, base, and windward and leeward curved surfaces. Prosser shows the pressure distribution and the force obtained by integrating the pressure on the front surface or the windward curved surface [9]. However, there is no report for the other two surfaces of a circular cylinder. Therefore, the results for a two-dimensional square cylinder are employed here as a reference [21–23]. First, the positive force acting in the normal direction of the front surface decreases as α increases [9]. Here, the direction to the inner of the cylinder is defined as the positive direction of forces. On the other hand, the pressure on the base increases with increasing α up to 14°, where intermittent reattachment of the shear layer is observed in the flow around the two-dimensional square cylinder [21,23]. The force acting on the windward curved surface is negative at α less than 45° [9]. The pressure is negative throughout this surface at α of less than 30°, even for a two-dimensional square cylinder [21,22]. Consequently, a force component acting in the negative direction of the x axis appears when $\alpha \neq 0^\circ$. Finally, the pressure increases with increasing α up to 20° on the leeward plane in the flow around the two-dimensional square cylinder [22]. Therefore, the force component acting in the positive direction of the x axis on this surface is weakened with increasing α. The discussion above implicates that the pressure on each surface is changed and that the drag force becomes smaller with increasing α in the range investigated. This leads to the decrease in C_{drag} due to increasing α. However, the clear difference in the C_{drag} curve by the flow reattachment on the side surface, which is observed in the case of a two-dimensional square cylinder, is not observed. The previous studies by Prosser [9] and Greenwell [20] also show that no clear change occurs in the curve of the drag coefficient between the case of the reattaching and nonreattaching flow for a circular and three-dimensional square cylinder, respectively.

Figure 9(b) shows that the lift force coefficients C_{lift} are negative at $\alpha \neq 0^\circ$ in the range investigated. This illustrates that the force acts in the negative direction of the z axis while the cylinder has angles to the freestream. As opposed to the case of C_{drag}, the absolute value at $\alpha = 10^\circ$ and the trends of C_{lift} curve are in good agreement with the result reported by Prosser, as shown in Fig. 9(b). The discussions for the lift force require taking into account the overall change in pressure on the four surfaces, as with the case of the drag force. Positive pressure distributes in a wide range of the front surface, and the force acting on the surface is positive regardless of α in the range considered [9]. Therefore, the force component in the negative direction of the z axis appears when $\alpha \neq 0^\circ$. However, the effect on the negative slope of the C_{lift} curve is considered to be very small because the force coefficient on the front surface decreases by approximately 0.05 from $\alpha = 0$ to 20° [9] and α is small. The pressure on the base is negative in the entire region [21,22] and the force component acting in the negative z direction occurs when $\alpha \neq 0^\circ$. However, the contribution to the negative gradient of the C_{lift} curve is considered to be small because the pressure on the base increases as α increases up to 14° in the case of the two-dimensional square cylinder [21,22]. The coefficient of the force acting on the windward curved surface is negative, and the coefficient is almost constant in the range that the flow does not reattach [9]. In contrast, the pressure on the leeward plane increases as α increases up to 14° while the pressure keeps a negative value [21,22]. Therefore, the pressure difference between these two side surfaces appears to be the main cause of the negative C_{lift} curve.

The C_{lift} curve shows a clear difference between the case of the nonreattaching and reattaching flow. The curve is linear in the case of the nonreattaching flow but it is nonlinear in the case of the reattaching flow. This change is reported in the study of the flow around a circular disk at low

Re_D. However, it appears at $\alpha = 35$–40° [24]. Furthermore, the curve shows that the slope of it is negative at $\alpha < 12^\circ$, and the slope is positive over $\alpha = 12^\circ$. This change of the slope of the C_{lift} curve is also observed in the case of a three-dimensional square cylinder [20], and the trend is quite similar. The negative slope is considered to be mainly caused by the pressure increase on the leeward curved surface in the case with $\alpha \leqslant 8^\circ$, as described above. Moreover, the slope of the C_{lift} curve is negative up to $\alpha = 12^\circ$. Hereafter, we discuss the reason why the negative slope appears after the flow reattachment and the C_{lift} recovery occurs. First, the relationship between the flow structure and the pressure on the side surface is discussed. The strong negative pressure region is formed by the separation bubble on the windward curved surface when the flow reattaches there. On the other hand, the relatively weak negative pressure compared to the case of the separation bubble is generated when the flow does not reattach. The flow separated at the leading edge seems to intermittently reattach on the side surface at $\alpha = 9$–11°, and the time during which the shear layer reattaches is presumed to become longer as α increases. Therefore, the time-averaged lift force is considered to be lower in the case of high α because the time during the separation bubble appearance is longer. The flow reattachment seems to steadily occur at $\alpha = 12^\circ$, and C_{lift} becomes the minimum. The positive slope of the C_{lift} curve over $\alpha = 12^\circ$ appears to be caused by the pressure recovery near the reattachment point and the weaker negative pressure, as with the case of a two-dimensional square cylinder [20–22].

The pitching moment coefficients C_{pitch} are negative at $\alpha \neq 0^\circ$ in the range considered, as shown in Fig. 9(c). The absolute value at $\alpha = 10^\circ$ in Prosser's work is 42.1% lower than in the present paper, but the trends of each C_{pitch} curve are similar. Negative C_{pitch} indicates that the pitching moment acts in the direction to recover the attitude of the cylinder to $\alpha = 0^\circ$. The front stagnation point locates at the center of the front surface of the cylinder in the case with $\alpha = 0^\circ$. The position of the stagnation point on the front surface moves to the upstream side when the freestream-aligned circular cylinder has angles [24]. This implies that the stagnation point approaches the windward curved surface. The location displacement of the stagnation point accompanies the change of the pressure distribution on the front surface [9,24]. The pressure near the stagnation point increases, on the other hand, the pressure on the opposite point across the center point of the front surface decreases. This pressure distribution change leads to generating the moment acting in the direction to recover the attitude [9,24]. The moment acting on the front surface in the direction to recover the attitude linearly increase, as shown in the paper by Prosser [9]. Similarly, the moment recovering attitude acts on the side surface where the shear layer approaches occur [9]. The results of a two-dimensional square cylinder showed that the base and the leeward curved surface do not have the pressure distribution which generates the moment to recover the attitude [21,22], and the contribution to the negative C_{pitch} is low.

The C_{pitch} curve shows that C_{pitch} linearly decreases, as shown in Fig. 9(c). Furthermore, the difference between the case of the nonreattaching and reattaching flow appears, as with the C_{lift} curve. The slope of the curve is large in the case of the reattaching flow compared to that in the case of nonreattaching flow. Prosser showed variation in the moment on the front surface and the windward curved surface [9]. The moment acting on the front surface varies with a constant gradient with respect to α in the range of the present paper. In contrast, the moment acting on the windward curved surface changes its slope after α at which the flow reattachment occurs. The combination of the effects on these two surfaces is considered to change the slope of the curve, as observed in Fig. 9(c).

B. Characteristic fluctuations

1. Fluctuations in velocity fields

Figure 10 shows the distributions of turbulent kinetic energy in the flow field at $\alpha = 0$–15 and $\mathrm{Re}_D = 3.3\times10^4$. The turbulent kinetic energy k at a position was calculated using

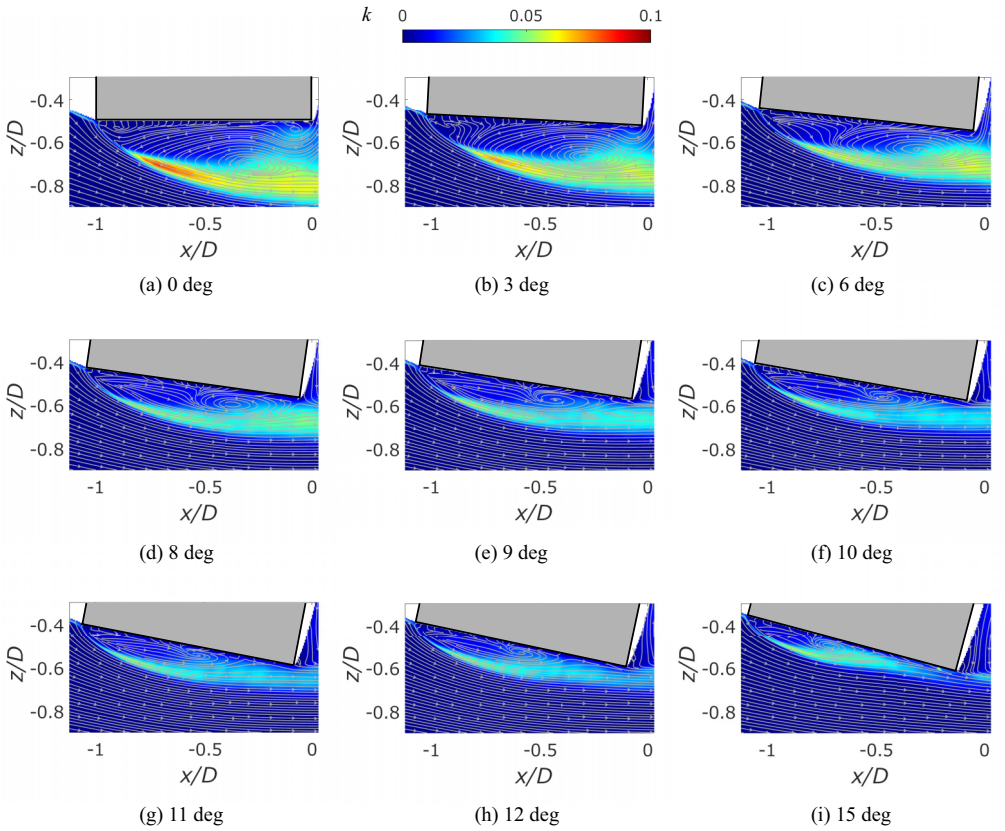

(a) 0 deg (b) 3 deg (c) 6 deg

(d) 8 deg (e) 9 deg (f) 10 deg

(g) 11 deg (h) 12 deg (i) 15 deg

FIG. 10. The distributions of the turbulent kinetic energy from (a) 0–(i) 15° at $\mathrm{Re}_D = 3.3\times10^4$. Gray lines with arrows in the figures represent the streamlines.

Eqs. (4)–(6):

$$k = \frac{1}{2}\sum_i (u_{i,\mathrm{RMS}}/U)^2, \tag{4}$$

$$u_{i,\mathrm{RMS}} = \sqrt{\frac{1}{n}\sum_{j=1}^{n} {u'_{i,j}}^2}, \tag{5}$$

$$u'_{i,j} = u_{i,j} - \frac{1}{n}\sum_{j=1}^{n} u_{i,j}, \tag{6}$$

where i $(= x, z)$, j, and n represent the axis of the velocity component, the index of an instantaneous velocity field in a series, and the number of instantaneous velocity fields in a series, respectively. The high k is distributed near the shear layer regardless of α. In the case of the nonreattaching flow with $\alpha = 0$–$8°$, the regions near the leading edge ($x/D = -0.8$–0.5) and the trailing edge have the higher k. They are caused by the Kelvin–Helmholtz (KH) instability which forms a vortex street and the positional fluctuations of the shear layer which are associated with the large-scale vortex shedding, respectively. Higher k is observed in the region near the leading edge as α decreases, which is considered to be because of the fluctuations by the KH vortices and the larger positional fluctuations of the shear layer. On the other hand, in the case of the reattaching flow with $\alpha \geqslant 9°$, k in the region near the leading edge is not varied by α. This suggests that the KH vortices appear

regardless of α, but the positional fluctuation does not occur. Lower k is observed in the region near the trailing edge as α increases in the case of the reattaching flow. Furthermore, k in the vicinity of the trailing edge gradually decreases from $\alpha = 9$ to 12° and is quite low at $\alpha = 15^\circ$. Since the positional fluctuations of the shear layer by the large-scale vortex shedding are greatly small or eliminated in the case of the reattaching flow [8], the velocity fluctuations near the trailing edge at $\alpha = 9$–12° seem to be caused by the intermittency of the flow reattachment and the change in the reattachment position. Therefore, the decrease in k there at $\alpha = 9$–12° implicates that the time of the reattachment is longer as α is higher because velocity fluctuations become small when a flow reattachment steadily occurs. In the case in which the intermittent flow reattachment appears, the negative pressure on the windward curved surface is considered to be stronger when the time during which the intermittent reattachment and corresponding separation bubble appear is longer, resulting in the lower C_{lift}. This has been discussed in Sec. IV A 2. The results shown in Fig. 10 support the discussion regarding C_{lift}.

2. Fluctuations in aerodynamic force

The power spectral densities (PSDs) of the lift force fluctuations at $\mathrm{Re}_D = 3.3\times10^4$ are shown in Fig. 11. The red and blue lines illustrate the PSDs in the wind-on and wind-off conditions, respectively. The PSD in the wind-off condition corresponds to the noise level of the aerodynamic force measurements. The spectrum at $\mathrm{St} > 0.25$ was neglected in the case of $\mathrm{Re}_D = 3.3\times10^4$ because of a high noise level. The distinct peak at $\mathrm{St} \approx 0.25$ shown in Figs. 11(i)–11(p) is considered to be caused by noise during the wind tunnel tests. Therefore, the peak is neglected in the discussion. The peak at $\mathrm{St} \approx 0.125$ is observed in the case of $\alpha = 0^\circ$, as shown in Fig. 11(a). The peak at the St is reported in the previous study [6], and this characteristic fluctuation relates to the large-scale vortex shedding. The peak at $\mathrm{St} \approx 0.125$ is observed in the case of the nonreattaching flow with $\alpha \leqslant 8^\circ$. However, it is not confirmed in the case of the reattaching flow at $\alpha \geqslant 9^\circ$. Prosser shows the root-mean-square (RMS) value of fluctuations of the side force [9] corresponding to the lift force in the present paper. The RMS value gradually decreases in the nonreattaching flow, but it becomes significantly small in the case of the reattaching flow. The previous reports referred to above and the results herein suggest that the aerodynamic force fluctuations in the lateral direction become small because the aerodynamic fluctuations associated with the large-scale vortex shedding do not occur by the change in flow behavior which is from the nonreattaching flow to the reattaching flow.

The previous studies [8,24,25] suggested that the lift force fluctuations are driven by the pressure fluctuations on the curved surface of a freestream-aligned circular cylinder. Yokota *et al.* discussed the relationship between the behavior of the shear layer and the pressure in the flow around a freestream-aligned circular cylinder and concluded that the pressure fluctuations on the curved surface generate the lift force fluctuations [8]. In addition, Yang *et al.* showed the PSDs of velocity fluctuations in the flow around the circular disk with $L/D = 0.2$. The peak at $\mathrm{St} = 0.122$ appears at $\mathrm{Re}_D = 300$ in the position near the shear layer. However, the spectrum of lift force fluctuations shows no characteristic peak at $\alpha = 0^\circ$ [24] while the velocity fluctuations are observed in the study by Yang *et al.* [25] Here, $\mathrm{Re}_D < 500$ in the study by Tian *et al.* [24]. These results indicate that the characteristic fluctuations of the lift force do not occur even though the pressure fluctuations occur in the flow around the circular disk which has extremely small or no area of the curved surface. Thus, the lift force fluctuations acting on the freestream-aligned circular cylinder without the flow reattachment are considered to be caused by the pressure fluctuations on the curved surface of the cylinder. The pressure fluctuations are also supposed to act important roles in the case of $\alpha \neq 0^\circ$, as in the case of $\alpha = 0^\circ$. There is no data on the pressure on the side surface, therefore, the following discussion is based on the analogy of the results of the two-dimensional square cylinder [21–23]. The high-pressure fluctuations are observed on the windward surface and the opposite surface, which accompanies the high fluctuations of the lift force [23]. The pressure fluctuations on the windward surface are small at $\alpha = 14^\circ$ where the intermittent flow reattachment appears. The changes in the strength of the pressure fluctuations by α are not significant in the case of $\alpha > 14^\circ$ [21–23]. The pressure fluctuations on the leeward surface also significantly decrease in the range

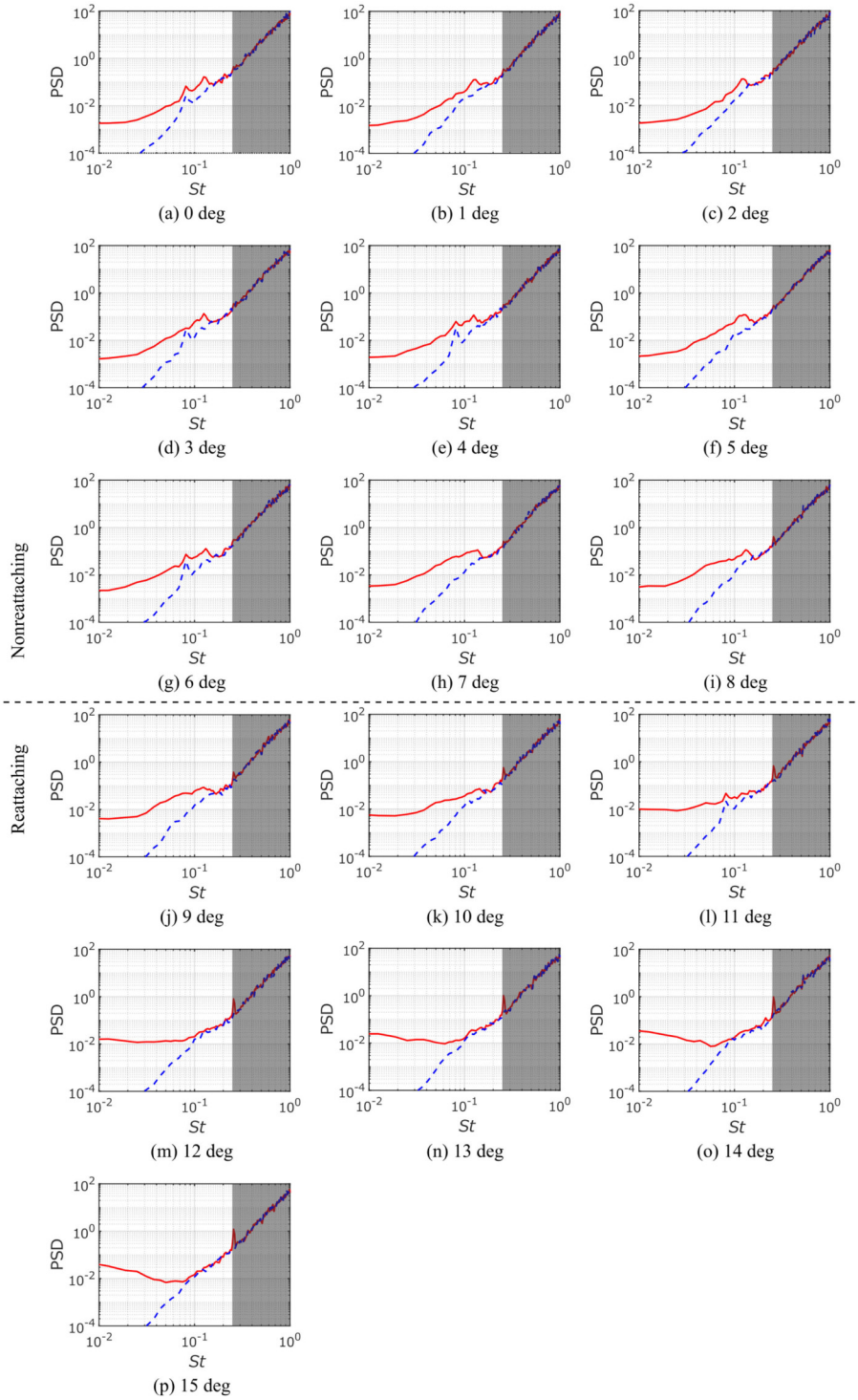

FIG. 11. The power spectral densities of the lift force fluctuations at (a) 0–(p) 15° at $\mathrm{Re}_D = 3.3\times10^4$. The red and blue lines in each figure illustrate the PSD in wind-on and wind-off condition, respectively. A region outside of interest is colored gray.

of $\alpha = 0$–14°. Therefore, the pressure fluctuations on the sides of the cylinder at $\alpha = 9^\circ$, where the intermittent flow reattachment is presumed to occur, appear smaller than those at $\alpha = 8^\circ$. The positional fluctuation of the shear layer on the windward side appears to be smaller in the case of reattachment flow, as mentioned in Sec. IV B 1. This implies that the pressure fluctuations between the shear layer and the cylinder are small. In short, the pressure fluctuations on the sides of the cylinder seem to generate the lift force fluctuations at $\alpha \neq 0^\circ$, and the fluctuations associated with the large-scale vortex shedding are observed in the nonreattaching flow at $\alpha \leqslant 8^\circ$. However, the fluctuations are not considered to be observed in the case of the reattaching flow at $\alpha \geqslant 9^\circ$.

We focus on the velocity field near the side surface where the shear layer approaches. Therefore, the flow structures behind the cylinder base cannot be discussed. In the case of the reattaching flow, the PSDs of the lift force fluctuations show no characteristic fluctuation associated with the large-scale vortex shedding, but it is not clarified whether a flow structure corresponding to the large-scale vortex shedding appears. Further investigation is required to clarify this point.

V. CONCLUSIONS

The effect of angle of attack α on the aerodynamic characteristics of a freestream-aligned circular cylinder with $L/D = 1.0$ was investigated, and the α where the flow separated at the leading edge of the cylinder reattaches was identified. The wind tunnel tests were conducted for the model levitated using the 0.3-m MSBS, and the flow field without support interference was realized. The α range was from 0 to 15°, and the aerodynamic forces and moments and the velocity field measurements focusing on the vicinity of the side surface of the cylinder were measured at each α by the MSBS and PIV, respectively. The α range with the flow reattachment was identified from the time-averaged velocity fields. The effect of α and the change in the flow field on the aerodynamic characteristics has been discussed using the curve of the time-averaged drag, lift, and pitching moment coefficients. In addition, the turbulent kinetic energy k and the PSDs of the lift force fluctuations were shown, and the effect of α on the fluctuations of the flow field and the lift force fluctuations has been discussed.

The flow fields are clarified to be classified into two states in the α range. One of them is observed at $\alpha \leqslant 8^\circ$, and the flow reattachment on the windward curved surface does not occur, which is called the nonreattaching flow. Another state is observed at $\alpha \geqslant 9^\circ$, and the flow reattachment occurs. This is called the reattaching flow. Here, the existence of the reattachment was judged from the presence of the separation of the flow on the base at the trailing edge.

The time-averaged drag coefficient C_{drag} decreases as α increases. However, the difference between the cases in the nonreattaching and reatatching flow was not observed. The time-averaged lift force acts in the negative direction of the z axis regardless of α, and the coefficient C_{lift} decreases at $\alpha = 0$–12° as α increases. Here, C_{lift} is the minimum at $\alpha = 12^\circ$, and it increases at further high α. The difference caused by the appearance of the flow reattachment is observed in the C_{lift} curve. The curve is linear in the case of the nonreattachng flow while it is nonlinear in the case of the reattaching flow. The time-averaged pitching moment acts to recover the attitude of the cylinder to $\alpha = 0^\circ$, and it becomes large at higher α. The C_{pitch} curve is linear regardless of α, but the slope of the curve is changed at $\alpha = 8$–9°. The slope in the case of the reattaching flow is larger than that in the case of the nonreattaching flow.

The larger velocity fluctuations near the shear layer are observed from the turbulent kinetic energy k distribution calculated from the instantaneous velocity fields, and it is high as α increases. In the case of the nonreattaching flow, the fluctuations are considered to be caused by the KH vortices and the positional fluctuations of the shear layer associated with the large-scale vortex shedding. In contrast, in the case of the reattaching flow, the KH vortices, the intermittency of the flow reattachment, and the change in the position of the reattachment appear to cause velocity fluctuations. Furthermore, the peak related to the large-scale vortex shedding in the PSD of the lift force fluctuations is confirmed in the case of the nonreattaching flow. However, no peak is observed except with the peak caused by the noise in the case of the reattaching flow. This might be

because the pressure fluctuations by the large-scale vortex shedding do not appear in the case of the reattaching flow.

The flow structure corresponding to the large-scale vortex shedding has not been directly captured from the velocity fields because the FOV of the PIV was focused on the shear layer reattachment. Since the wake of the circular cylinder with α is not an axial flow as opposed to the case of the freestream-aligned circular cylinder, the measurement plane parallel to the freestream is not suitable to address a discussion on it. However, the velocity field measurement on the plane perpendicular to the freestream is quite difficult because the optical setup is limited by the physical interference of the coil system of the MSBS. Therefore, comprehension of the phenomena by analyses using the Fourier transform and mode decomposition of two-dimensional three-component velocity data on the plane perpendicular to the freestream is left for future work.

ACKNOWLEDGMENT

This work was supported by JSPS KAKENHI (Grants No. 18H03809, No. 21H04586, and No. 21J20673).

The authors have no conflicts to disclose.

APPENDIX A: UNCERTAINTY OF VELOCITY

The velocity fields calculated by the SPC and CSC methods from the particle images taken by the PIV measurements have uncertainty. In particular, the α where the flow reattachment occurs is identified from the time-averaged velocity field, therefore, uncertainty analysis is important.

The methods to evaluate the uncertainty for the velocity fields obtained by the SPC and CSC are the same as those in the previous study [8]. The distribution of the uncertainty of the time-averaged velocity $P_{\overline{u_i}/U}$ was calculated from the four fields. Each field was obtained from 5000 particle images using the SPC method. The RMS values of the four fields were assumed as the $P_{\overline{u_i}/U}$ distribution. Figure 12 shows the uncertainty distribution of the time-averaged velocity field for each component at $\mathrm{Re}_D = 3.3\times10^4$ and $\alpha = 0^\circ$. The uncertainty of the instantaneous velocity $P_{u_i/U}$ was calculated by Dynamic Studio. Figure 13 shows the distributions of the RMS values of the uncertainty for each component at $\mathrm{Re}_D = 3.3\times10^4$ and $\alpha = 0^\circ$.

APPENDIX B: UNCERTAINTY OF AERODYNAMIC FORCE AND MOMENT COEFFICIENTS

The aerodynamic force and moment coefficients are calculated using the values of measured forces and moments, dynamic pressure, and the dimension of the model. Therefore, the uncertainty

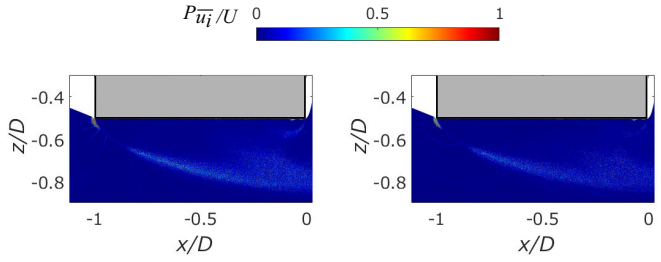

(a) Uncertainty of $\overline{u_x}/U$ (b) Uncertainty of $\overline{u_z}/U$

FIG. 12. Uncertainty of the time-averaged velocity in (a) the x direction and (b) the z direction in the case with $\mathrm{Re}_D = 3.3\times10^4$ and $\alpha = 0^\circ$.

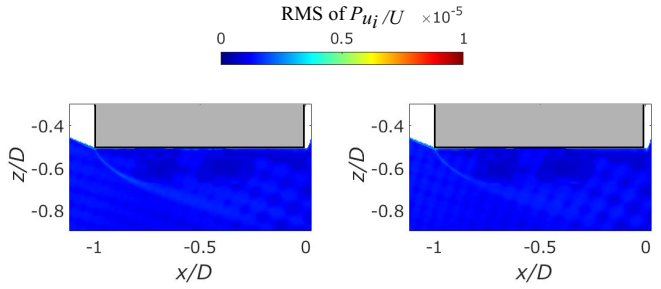

(a) Uncertainty of u_x/U (b) Uncertainty of u_z/U

FIG. 13. RMS values of uncertainty of the instantaneous velocity in (a) the x direction and (b) the z direction in the case with $\mathrm{Re}_D = 3.3\times10^4$ and $\alpha = 0^\circ$.

for them($\Delta C_{\mathrm{force}}$ and $\Delta C_{\mathrm{moment}}$) can be estimated by the following equation:

$$\left(\frac{\Delta C_{\mathrm{force}}}{C_{\mathrm{force}}}\right)^2 = \left(\frac{\Delta F}{F}\right)^2 + \left(\frac{\Delta q}{q}\right)^2 + \left(\frac{\Delta S}{S}\right)^2, \tag{B1}$$

$$\left(\frac{\Delta C_{\mathrm{moment}}}{C_{\mathrm{moment}}}\right)^2 = \left(\frac{\Delta N}{N}\right)^2 + \left(\frac{\Delta q}{q}\right)^2 + \left(\frac{\Delta S}{S}\right)^2 + \left(\frac{\Delta L}{L}\right)^2, \tag{B2}$$

where ΔF and ΔN are twice the standard deviations of errors in the force calibration test. These values are summarized in Table I. Here, Δq is the standard deviation of the error of the dynamic pressure, which is 3.02 Pa. This is obtained by the accuracy of the fine differential pressure gauge used in the wind tunnel tests and the ratio of contraction of T-BART, which are 3 Pa and 12.96, respectively. In addition, ΔS and ΔL are the standard deviations of the errors of the projection area onto yz plane and the length of the model, respectively. These are related to the process of making the model, including machining and painting. Those errors of ΔS and ΔL were calculated by assuming that the diameter and length of the model after the processing were within 0.2 mm of the designated dimensions.

APPENDIX C: TRANSFORMATION TO OBTAIN EQS. (C9) AND (C10)

This Appendix presents the process of calculation of the aerodynamic forces and moments. Equations (C1) and (C2) represent forces and moments acting on a model, respectively,

$$\begin{bmatrix} F_x \\ F_y \\ F_z \end{bmatrix} = \begin{bmatrix} h_{xx}I_{\mathrm{drag}} & h_{xy}I_{\mathrm{side}} & h_{xz}I_{\mathrm{lift}} \\ h_{xy}I_{\mathrm{side}} & -\frac{1}{2}h_{xx}I_{\mathrm{drag}} & 0 \\ h_{xz}I_{\mathrm{lift}} & 0 & -\frac{1}{2}h_{xx}I_{\mathrm{drag}} \end{bmatrix} \begin{bmatrix} M_x \\ 0 \\ 0 \end{bmatrix}, \tag{C1}$$

$$\begin{bmatrix} N_x \\ N_y \\ N_z \end{bmatrix} = \begin{bmatrix} 0 & h_zI_{\mathrm{pitch}} & -h_yI_{\mathrm{yaw}} \\ -h_zI_{\mathrm{pitch}} & 0 & 0 \\ h_yI_{\mathrm{yaw}} & 0 & 0 \end{bmatrix} \begin{bmatrix} M_x \\ 0 \\ 0 \end{bmatrix}, \tag{C2}$$

where h_i and h_{ij} $(i, j = x, y, z)$ are magnetic field intensity per electric current and the component of its gradient in each direction, respectively. The subscripts of x, y, and z represent the axes, and I_{drag}, I_{side}, I_{lift}, I_{pitch}, and I_{yaw} are the electric current for the control of the position and attitude of the model. Here, two assumptions are applied to calculate the forces and moments. The first one is that the permanent magnet has a magnetic moment only in the axial direction of it (M_x), and another one is that the coordinate system of the MSBS and that of the model matches in the case of $\alpha = 0^\circ$.

TABLE I. Standard deviation of error of estimated forces and moments in the calibration test.

Axis	Standard deviation
x	1.67×10^{-3} N
y	5.06×10^{-4} N
z	8.20×10^{-4} N
θ	2.42×10^{-5} N m
ψ	1.64×10^{-5} N m

The relationship between the coordinate system of the MSBS and that of the model is written as represented in Eqs. (C3),

$$\begin{bmatrix} x_{\mathrm{model}} \\ y_{\mathrm{model}} \\ z_{\mathrm{model}} \end{bmatrix} = \begin{bmatrix} 1 & 0 & 0 \\ 0 & \cos\phi & \sin\phi \\ 0 & -\sin\phi & \cos\phi \end{bmatrix} \begin{bmatrix} \cos\theta & 0 & -\sin\theta \\ 0 & 1 & 0 \\ \sin\theta & 0 & \cos\theta \end{bmatrix} \begin{bmatrix} \cos\psi & \sin\psi & 0 \\ -\sin\psi & \cos\psi & 0 \\ 0 & 0 & 1 \end{bmatrix} \begin{bmatrix} x_{\mathrm{MSBS}} \\ y_{\mathrm{MSBS}} \\ z_{\mathrm{MSBS}} \end{bmatrix}, \tag{C3}$$

where x_{model}, y_{model}, and z_{model} are positions in the coordinate system of the model, and x_{MSBS}, y_{MSBS}, and z_{MSBS} are positions in the coordinate system of the MSBS. Since the model was supported with angles in the pitching direction, the components of the magnetic moment of the permanent magnet in the coordinate system of the MSBS are expressed as follows:

$$\begin{bmatrix} M'_x \\ M'_y \\ M'_z \end{bmatrix} = \begin{bmatrix} \cos\theta & 0 & \sin\theta \\ 0 & 1 & 0 \\ -\sin\theta & 0 & \cos\theta \end{bmatrix} \begin{bmatrix} M_x \\ 0 \\ 0 \end{bmatrix}. \tag{C4}$$

This is substituted in Eqs. (C1) and (C2):

$$\begin{bmatrix} F_x \\ F_y \\ F_z \end{bmatrix} = \begin{bmatrix} h_{xx}I_{\mathrm{drag}} & h_{xy}I_{\mathrm{side}} & h_{xz}I_{\mathrm{lift}} \\ h_{xy}I_{\mathrm{side}} & -\frac{1}{2}h_{xx}I_{\mathrm{drag}} & 0 \\ h_{xz}I_{\mathrm{lift}} & 0 & -\frac{1}{2}h_{xx}I_{\mathrm{drag}} \end{bmatrix} \begin{bmatrix} \cos\theta & 0 & \sin\theta \\ 0 & 1 & 0 \\ -\sin\theta & 0 & \cos\theta \end{bmatrix} \begin{bmatrix} M_x \\ 0 \\ 0 \end{bmatrix}, \tag{C5}$$

$$\begin{bmatrix} N_x \\ N_y \\ N_z \end{bmatrix} = \begin{bmatrix} 0 & h_zI_{\mathrm{pitch}} & -h_yI_{\mathrm{yaw}} \\ -h_zI_{\mathrm{pitch}} & 0 & 0 \\ h_yI_{\mathrm{yaw}} & 0 & 0 \end{bmatrix} \begin{bmatrix} \cos\theta & 0 & \sin\theta \\ 0 & 1 & 0 \\ -\sin\theta & 0 & \cos\theta \end{bmatrix} \begin{bmatrix} M_x \\ 0 \\ 0 \end{bmatrix}. \tag{C6}$$

A transformation of these equations results in the following equation:

$$\begin{bmatrix} F_x \\ F_y \\ F_z \end{bmatrix} = \begin{bmatrix} h_{xx}I_{\mathrm{drag}} & h_{xy}I_{\mathrm{side}} & h_{xz}I_{\mathrm{lift}} \\ h_{xy}I_{\mathrm{side}} & -\frac{1}{2}h_{xx}I_{\mathrm{drag}} & 0 \\ h_{xz}I_{\mathrm{lift}} & 0 & -\frac{1}{2}h_{xx}I_{\mathrm{drag}} \end{bmatrix} \begin{bmatrix} M_x\cos\theta \\ 0 \\ -M_x\sin\theta \end{bmatrix}, \tag{C7}$$

$$\begin{bmatrix} N_x \\ N_y \\ N_z \end{bmatrix} = \begin{bmatrix} 0 & h_zI_{\mathrm{pitch}} & -h_yI_{\mathrm{yaw}} \\ -h_zI_{\mathrm{pitch}} & 0 & 0 \\ h_yI_{\mathrm{yaw}} & 0 & 0 \end{bmatrix} \begin{bmatrix} M_x\cos\theta \\ 0 \\ -M_x\sin\theta \end{bmatrix}. \tag{C8}$$

Equations (C9) and (C10) are derived by transforming Eqs. (C7) and (C8), respectively:

$$\begin{bmatrix} F_x \\ F_y \\ F_z \end{bmatrix} = \begin{bmatrix} A_{\text{drag}} \cos\theta & 0 & -A_{\text{lift}} \sin\theta \\ 0 & A_{\text{side}} \cos\theta & 0 \\ \frac{1}{2} A_{\text{drag}} \sin\theta & 0 & A_{\text{lift}} \cos\theta \end{bmatrix} \begin{bmatrix} I_{\text{drag}} \\ I_{\text{side}} \\ I_{\text{lift}} \end{bmatrix}, \tag{C9}$$

$$\begin{bmatrix} N_x \\ N_y \\ N_z \end{bmatrix} = \begin{bmatrix} 0 & 0 & A_{\text{yaw}} \sin\theta \\ 0 & A_{\text{pitch}} \cos\theta & 0 \\ 0 & 0 & A_{\text{yaw}} \cos\theta \end{bmatrix} \begin{bmatrix} 0 \\ I_{\text{pitch}} \\ I_{\text{yaw}} \end{bmatrix}, \tag{C10}$$

where the following relationships are used. The specific value of A for each direction is obtained from the gradient of the line shown in Fig. 6:

$$\begin{aligned} A_{\text{drag}} &= M_x h_{xx} = -0.10296 \text{ N/A}, \\ A_{\text{side}} &= M_x h_{xy} = -0.21327 \text{ N/A}, \\ A_{\text{lift}} &= M_x h_{xz} = -0.65824 \text{ N/A}, \\ A_{\text{pitch}} &= -M_x h_z = -0.06555 \text{ Nm/A}, \\ A_{\text{yaw}} &= M_x h_y = -0.02101 \text{ Nm/A}. \end{aligned}$$

[1] E. Berger, D. Scholz, and M. Schumm, Coherent vortex structures in the wake of a sphere and a circular disk at rest and under forced vibrations, J. Fluids Struct. **4**, 231 (1990).

[2] H. Higuchi, P. Van Langen, H. Sawada, and C. E. Tinney, Axial flow over a blunt circular cylinder with and without shear layer reattachment, J. Fluids Struct. **22**, 949 (2006).

[3] H. Higuchi, H. Sawada, and H. Kato, Sting-free measurements on a magnetically supported right circular cylinder aligned with the free stream, J. Fluid Mech. **596**, 49 (2008).

[4] T. Nonomura, K. Sato, K. Fukata, H. Nagaike, H. Okuizumi, Y. Konishi, K. Asai, and H. Sawada, Effect of fineness ratios of 0.75–2.0 on aerodynamic drag of freestream-aligned circular cylinders measured using a magnetic suspension and balance system, Exp. Fluids **59**, 77 (2018).

[5] K. Shinji, H. Nagaike, T. Nonomura, K. Asai, H. Okuizumi, Y. Konishi, and H. Sawada, Aerodynamic characteristics of low-fineness-ratio freestream-aligned cylinders with magnetic suspension and balance system, AIAA J. **58**, 3711 (2020).

[6] S. Yokota, T. Ochiai, Y. Ozawa, T. Nonomura, and K. Asai, Analysis of unsteady flow around an axial circular cylinder of critical geometry using combined synchronous measurement in magnetic suspension and balance system, Exp. Fluids **62**, 15 (2021).

[7] M. Kuwata, Y. Abe, S. Yokota, T. Nonomura, H. Sawada, A. Yakeno, K. Asai, and S. Obayashi, Flow characteristics around extremely low fineness-ratio circular cylinders, Phys. Rev. Fluids **6**, 054704 (2021).

[8] S. Yokota, K. Asai, and T. Nonomura, Instability of separated shear layer around levitated freestream-aligned circular cylinder, Phys. Fluids **34**, 064104 (2022).

[9] D. T. Prosser, Advanced computational techniques for unsteady aerodynamic-dynamic interactions of bluff bodies, Ph.D. thesis, Georgia Institute of Technology, 2015.

[10] D. T. Prosser and M. J. Smith, Numerical characterization of three-dimensional bluff body shear layer behaviour, J. Fluid Mech. **799**, 1 (2016).

[11] K. Tashiro, S. Yokota, F. Zigunov, Y. Ozawa, K. Asai, and T. Nonomura, Slanted cylinder afterbody aerodynamics measured by 0.3-m magnetic suspension and balance system with six-degrees-of-freedom control, Exp. Fluids **63**, 119 (2022).

[12] K. Endo, T. Ambo, Y. Saito, T. Nonomura, L. Chen, and K. Asai, Proposal and verification of optical flow reformulation based on variational method for skin-friction-stress field estimation from unsteady oil film distribution, J. Visualization **25**, 263 (2022).
[13] C. E. Willert and M. Gharib, Digital particle image velocimetry, Exp. Fluids **10**, 181 (1991).
[14] J. Westerweel, P. Geelhoed, and R. Lindken, Single-pixel resolution ensemble correlation for micro-PIV applications, Exp. Fluids **37**, 375 (2004).
[15] Y. Ozawa, T. Ibuki, T. Nonomura, K. Suzuki, A. Komuro, A. Ando, and K. Asai, Single-pixel resolution velocity/convection velocity field of a supersonic jet measured by particle/schlieren image velocimetry, Exp. Fluids **61**, 129 (2020).
[16] T. Nonomura, Y. Ozawa, T. Ibuki, K. Nankai, A. Komuro, H. Nishida, M. Kotsonis, N. Kubo, and H. Kawabata, Single-pixel particle image velocimetry for characterization of dielectric barrier discharge plasma actuators, AIAA J. **58**, 4952 (2020).
[17] S. Scharnowski, R. Hain, and C. J. Kähler, Reynolds stress estimation up to single-pixel resolution using piv-measurements, Exp. Fluids **52**, 985 (2012).
[18] T. Nonomura, T. Ibuki, Y. Ozawa, K. Asai, and A. Oyama, Generalized estimation methods of turbulent fluctuation of high-speed flow with single-pixel resolution particle image velocimetry, Meas. Sci. Technol. **32**, 125306 (2021).
[19] H. Senda, H. Sawada, H. Okuizumi, Y. Konishi, and S. Obayashi, Aerodynamic measurements of AGARD-B model at high angles of attack by 1-m magnetic suspension and balance system, in *Proceedings of the 2018 AIAA Aerospace Sciences Meeting* (American Institute of Aeronautics and Astronautics, Kissimmee, Florida, 2018), p. 0302.
[20] D. Greenwell, Modelling of static aerodynamics of helicopter underslung loads, Aeronaut. J. **115**, 201 (2011).
[21] Y. Nishimura and Y. Taniike, Fluctuating wind forces on a stationary two-dim. square prism, in *Proceedings of the 16th National Symposium of Wind Engineering* (Japan Association for Wind Engineering, Tokyo, 2000), pp. 255–260.
[22] S. Oka, T. Ishihara, and Y. Fujino, Numerical study of aerodynamic force and surface pressure of square prism in a uniform flow, in *Proceedings of the 17th National Symposium of Wind Engineering* (Japan Association for Wind Engineering, Tokyo, 2002), pp. 36–36.
[23] T. Ishihara, S. Oka, and Y. Fujino, Numerical study of aerodynamic characteristics of square prism in a uniform flow, Doboku Gakkai Ronbunshuu A **62**, 78 (2006).
[24] X. Tian, Z. Hu, H. Lu, and J. Yang, Direct numerical simulations on the flow past an inclined circular disk, J. Fluids Struct. **72**, 152 (2017).
[25] J. Yang, M. Liu, G. Wu, Q. Liu, and X. Zhang, Low-frequency characteristics in the wake of a circular disk, Phys. Fluids **27**, 064101 (2015).